P-MAPS: A Custom-Topology Velostat Insole for Pressure Redistribution in Diabetic Foot Care

Andres Osorio Salazar, *Member, IEEE*, Maël Dagon, Paolo Germano, Christian Koechli, Zoltan Pataky, Yoan Civet, and Yves Perriard, *Senior Member, IEEE*

***Abstract*—Diabetic foot ulcers (DFUs) remain a major complication of diabetes mellitus, with significant human and economic costs. Plantar pressure (PP) is the most widely used surrogate to assess DFU risk. Existing PP measurement insoles are primarily designed for in-clinic assessments using external instrumentation to guide passive offloading strategies. However, reliance on brief clinical measurements limits their ability to capture real-world loading patterns, motivating the development of sensing systems capable of continuous monitoring and integration within pressure-management footwear. Such systems require spatially discretized sensing elements fully embedded within the shoe architecture. This work presents the design and characterization of plantar-monitoring Au-plated pressure system (P-MAPS), a custom-topology pressure-sensing insole codesigned for precise spatial alignment with offloading elements. The sensor uses the piezoresistive response of Velostat combined with gold-plated electrodes to improve uniformity and repeatability. The device exhibits a measurement range of 45–350 kPa, a coefficient of variation below 2.5%, normalized hysteresis of 25.8%, and 6% drift after 5 min. Dynamic gait validation against a commercial reference (Pedar, Novel) demonstrated accurate peak pressure estimation with 2.6% error under full spatial overlap while enabling localized pressure measurement over actuated regions and revealing that sensing areas not colocated with actuator regions can misrepresent local pressures due to spatial averaging effects. These results establish P-MAPS as a robust and practical sensing solution for continuous, footwear-integrated plantar-pressure monitoring and adaptive offloading applications.**

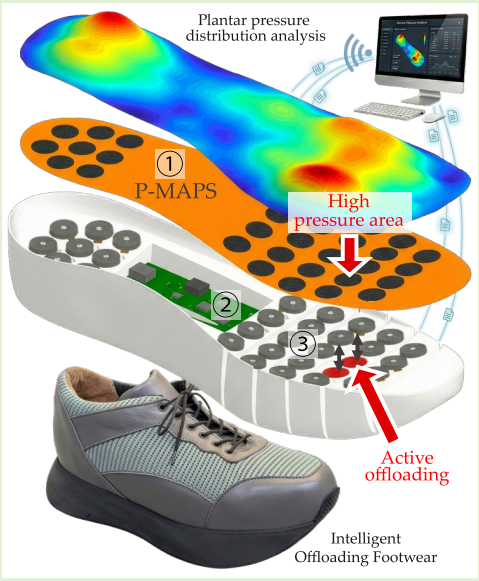

***Index Terms*—Diabetic foot ulceration, piezoresistive devices, plantar-pressure (PP) sensors, pressure sensors, wearable sensors.**

I. Introduction

DIABETES mellitus is a global health crisis that affects an estimated 589 million adults worldwide (2025), a figure projected to increase to 853 million by 2050 [1]. Among its complications, diabetic foot ulcers (DFUs) are particularly severe and costly to both patients and healthcare systems. Up to 25% of people with diabetes will develop a foot ulcer during their lifetime [2]. Approximately 5% of patients require amputation within one year of ulcer onset, and DFUs are associated with a five-year mortality rate of nearly 40% [3].

The development of DFUs is the result of multiple interrelated biomechanical and physiological factors, with neuropathy (nerve damage) being one of the main contributors. Neuropathy, present in nearly 50% of patients with diabetes [4], leads to a cascade of complications. Motor impairment contributes to limited joint mobility and foot deformities that increase mechanical stress, while sensory loss reduces protective feedback and increases the likelihood of unnoticed injuries. Together, these conditions promote callus formation, tissue breakdown, and ultimately ulcer development [4].

Received 31 March 2026; accepted 9 April 2026. Date of publication 21 April 2026; date of current version 2 June 2026. This work was supported by the Innosuisse-Swiss Innovation Agency Program under Grant 107.872 IP-ENG. The associate editor coordinating the review of this article and approving it for publication was Dr. Wei Xu. *(Corresponding author: Andres Osorio Salazar.)*

This work involved human subjects in its research. Approval of all ethical and experimental procedures and protocols was granted by the Human Research Ethics Committee at the Ecole polytechnique fédérale de Lausanne (EPFL) under Approval No: HREC000567/2024 and performed in line with EPFL requirements.

Andres Osorio Salazar, Maël Dagon, Paolo Germano, Christian Koechli, Yoan Civet, and Yves Perriard are with Ecole polytechnique fédérale de Lausanne (EPFL), 2000 Neuchatel, Switzerland (e-mail: andres.osoriosalazar@epfl.ch).

Zoltan Pataky is with the Unit of Therapeutic Patient Education, WHO Collaborating Centre, Geneva University Hospitals, 1205 Geneva, Switzerland, and also with the Faculty Diabetes Center, Faculty of Medicine, University of Geneva, 1205 Geneva, Switzerland.

Digital Object Identifier 10.1109/JSEN.2026.3684148

Because these neuropathic changes alter gait, load distribution, and tissue tolerance, continuous monitoring and reduction of mechanical stress are essential to better understand and mitigate ulcer risk. With the long-term objective of developing footwear that effectively and autonomously manages plantar stress in patients with diabetes, our group has developed intelligent offloading footwear (IOF) [5] to address this need. Its functionality relies on three main components: (1) plantar-pressure (PP) monitoring; (2) pressure-redistribution algorithm; and (3) pressure redistribution microactuator array. In this article, we focus on the PP-monitoring component (1).

PP is widely recognized as an important metric for assessing foot-loading patterns and identifying areas subjected to elevated mechanical stress in patients at risk of developing DFUs. Early studies, such as Veves et al. [6], showed that individuals exhibiting higher PP are more likely to develop complications compared to those with normal pressure levels. As a result, accurate PP measurements have become essential in applications ranging from DFU risk assessment to the design of pressure-redistributing interventions [7].

Various mechanical offloading strategies have been developed to reduce plantar stress in patients with diabetic neuropathy, including custom-made insoles, rocker-bottom footwear, total-contact casts, and other orthotic interventions [6], [7]. Custom orthotic insoles have been shown to effectively redistribute PP in patients with neuropathy and foot deformities [15]. However, these approaches are typically passive and optimized through iterative clinical adjustments rather than continuous feedback from daily activities, meaning that pressure redistribution during fitting may not fully reflect real-world loading conditions.

Reliable pressure measurements are therefore essential to guide offloading interventions, placing stringent requirements on the performance and integration of pressure-sensing systems. However, conventional assessments are based on brief clinic-based measurements that do not reflect the pressures encountered during everyday walking, climbing stairs, or uneven terrain. This limitation highlights the need for wearable sensing systems capable of providing accurate, repeatable, long-term PP data for real-time offloading strategies.

Reported sensing insoles exhibit a wide range of performance characteristics. Commercial systems typically employ dense sensor arrays with full-scale ranges of several hundred kilopascals, while research prototypes often adopt smaller numbers of targeted sensing regions for clinically relevant plantar locations [16], [17], [18]. Sampling rates vary from a few tens of hertz in wearable systems to several hundred hertz in laboratory gait analysis platforms. In practice, system performance strongly depends on sensor distribution, mechanical integration, and calibration strategies, and important metrics such as repeatability, hysteresis, and drift are not consistently reported across studies [16], [17].

From the commercial sensing insole systems available for capturing PP data, Pedar (Novel GmbH) [8], F-Scan GO (Tekscan) [9], and Moticon OpenGo [10] are the most well known. These systems provide high-resolution and reliable PP measurements and have been widely used in clinical studies. However, integrating them into IOF remains challenging because their external electronics increase user burden and their fixed sensor layouts cannot easily align with actuator positions required for targeted pressure redistribution.

Numerous studies have investigated custom-made pressure-sensing insoles using capacitive, photoelectric, fiber-Bragg-grating, inductive, optical, piezoelectric, and piezoresistive technologies. Each approach offers advantages but also trade-offs for thin wearable implementations. Capacitive sensors provide high sensitivity but can suffer from parasitic capacitances and environmental sensitivity [11], [19], [20]. Optical and photoelectric systems enable high spatial resolution but increase thickness and system complexity [21], [22]. Fiber-Bragg-grating sensors provide excellent multiplexing capability but require costly interrogation units [23]. Inductive sensors rely on stable coil geometries that are difficult to maintain on deformable substrates [24]. Piezoelectric sensors are well suited for dynamic measurements but less suitable for static or slowly varying plantar loads due to charge leakage [25], [26].

Piezoresistive sensors provide a favorable compromise between mechanical compliance, fabrication simplicity, and electronic integration, enabling direct measurement of static and quasi-static PP with minimal circuitry and low cost [17], [18]. Current research focuses on polymer-based composites, including carbon-filled thermoplastic films (e.g., Velostat), carbon-black elastomers (e.g., PDMS-CB) [27], CNT- or graphene-enhanced elastomers [28], [29], conductive textiles (e.g., EeonTex) [30], and printed conductive inks. Although nanocarbon composites can offer higher sensitivity, they typically require more complex fabrication, whereas carbon-filled polyethylene films offer a practical balance between cost, availability, and mechanical robustness [16], [17].

Table I summarizes representative plantar-pressure-sensing systems reported in the literature, including commercial platforms such as Pedar [8], F-Scan [9], and Moticon OpenGo [10], as well as research-oriented systems [11], [12], [13], [14]. The systems are compared in terms of sensing principle, operating pressure range, sensor density, thickness, hysteresis, sampling performance, sensing topology, and level of footwear integration. As shown in Table I, existing solutions typically rely on external acquisition modules or employ sensing layouts optimized for general gait analysis. In contrast, sensing approaches that enable customized topologies aligned with offloading modules and seamless integration within footwear are required, while maintaining sensing performance comparable to existing wearable plantar-pressure monitoring systems.

Developing stable, manufacturable, and fully integrated sensing/actuating solutions remains a challenge. To address these limitations, we developed a new sensing architecture that improves measurement stability, manufacturability, and integration within IOF. The present work introduces a piezoresistive insole that uses Velostat as the sensing material and gold-plated electrodes to achieve improved uniformity and drift performance. The manufacturing approach has been simplified by employing a continuous piezoresistive layer, eliminating the need to individually bond material segments

TABLE I
COMPARISON OF REPRESENTATIVE PLANTAR-PRESSURE-SENSING INSOLES REPORTED IN THE LITERATURE WITH THE PROPOSED P-MAPS SYSTEM. N/R: NOT REPORTED IN THE CITED REFERENCE

System / Reference	Sensing Principle	Pressure Range (kPa)	Sensing Regions	Pitch (mm)	Thickness (mm)	Hysteresis (%)	Sampling Rate (Hz)	Topology Alignment	Footwear Integration
Commercial systems									
Pedar (Novel GmbH) [8]	Capacitive	15–600	99–175	∼7	1.9	< 7	50, 100, 400	Fixed	External module
F-Scan GO (Tekscan) [9]	Resistive	0–862	< 966	∼5	0.28	N/R	< 500	Fixed	External module
Moticon OpenGo [10]	Capacitive	N/R	16	N/R	N/R	N/R	5–50	Fixed	Fully integrated
Research systems									
Tang et al. [11]	Capacitive	0–300 -90–90	4, inc. shear	N/R	< 3	N/R	100	Custom	Wearable electronics
Tiwari et al. [12]	Piezoresistive	< 960	31	20	N/R	N/R	20	Custom	Embedded prototype
de Fazio et al. [13]	Piezoresistive	0–500	8	N/R	N/R	N/R	5	Custom	Wearable electronics
Hu et al. [14]	Piezoresistive	0–400	174	7.5	N/R	N/R	50	Custom	Wearable electronics
Proposed system									
This work (P-MAPS)	**Piezoresistive**	**45–350**	**31**	**20**	∼0.5–2	**25.8**	**50**	**Custom**	**Embedded IOF**

to each electrode and significantly improving manufacturing reliability. The new insole has a 31-region array with sensing areas of 78.5 mm^2 and a pitch of 15–20 mm, coincident with the offloading components, while offering a measurement range of up to 350 kPa, parameters selected to meet the active offloading requirements described in [5] for the prevention of DFU. This development represents an advance in practical usability, measurement stability, and readiness for integration into autonomous offloading systems.

In Section II, the design and operating principle of the insole are presented. Section III describes the test-bench characterization, and Section IV demonstrates gait measurements. Finally, Section V summarizes the conclusions and future work.

II. CONCEPTUAL DESIGN

A. Functional Requirements

Based on our previous work [12], the following functional requirements are listed.

1) High bending compliance, with a bending radius smaller than 15 cm and without surface irregularities.
2) The 31 sensing areas corresponding to the topology of the IOF offloading regions [5], each covering at least 50% of the actuator area.
3) Sensing range of 50–300 kPa and resolution of 10 kPa throughout the range.

The previously stated high-linearity requirement was found to be not necessary, given that with the available computation power, it would be possible to manage a polynomial approximation as a calibration curve. Similarly, the wide sensing range of 960 kPa was updated to at least 300 kPa, since any measurement above 250 kPa, the conventional threshold for ulceration risk, would trigger the offloading action in any case, so measurements beyond this threshold would not be required in our application. This change highlights one of the main differences between a sensing insole used for data acquisition (DAQ) only and one used for active offloading.

B. Concept

The proposed design, named the plantar-monitoring Au-plated pressure system (P-MAPS), consists of a piezoresistive layer sandwiched between two Au (gold)-plated electrodes fabricated as conventional flexible printed circuit boards (PCBs) with polyimide as the base substrate, as shown in Fig. 1(a). The sensing stack is encapsulated throughout its perimeter using a pressure-sensitive adhesive laminate (PSA). The resistance of the material is measured between the + and − electrodes throughout its thickness ($S_1, \ldots, S_{31}$). Although gold plating reduces the overall resistance of the system, making precise measurement more challenging, it also prevents electrode oxidation, which can otherwise introduce resistance variability. As such, gold-plated electrodes contribute to more stable and reliable measurements. The topology of the electrodes and, therefore, of the sensing areas is aligned with that of the offloading actuators ($A_1, \ldots, A_{31}$), allowing PP readings directly above each actuator and facilitating both the detection of high-pressure regions in and the development of effective offloading algorithms.

The piezoresistive material of choice was Velostat, for its high availability, uniformity, and low tendency to drift. The stack was built using a layer of Velostat that covers the entirety of the flexible PCB, rather than only individual electrodes, for the sake of manufacturing simplicity. Additionally, the insole also featured an ethylene-vinyl acetate (EVA) foam layer that is attached using double-sided tape to the underside of the heel region, with holes that allow the sensing areas to directly contact the offloading actuators, and maintains the sensing insole aligned, which is visible in Fig. 1(a), both in the top and bottom schematics.

The composition of the sensing insole layers is shown in Fig. 1(a), and the electronic circuit used for DAQ is included in Fig. 1(b). In both figures, a common electrode layer (L3), a piezoresistive layer (L2), and an individual electrode layer (L1) are represented. In Fig. 1(b), the left operational amplifier provides to L3 a negative voltage common level (reference voltage) that depends on the 12-bit output of the microcontroller (μC, model STM32U585VIT6 from

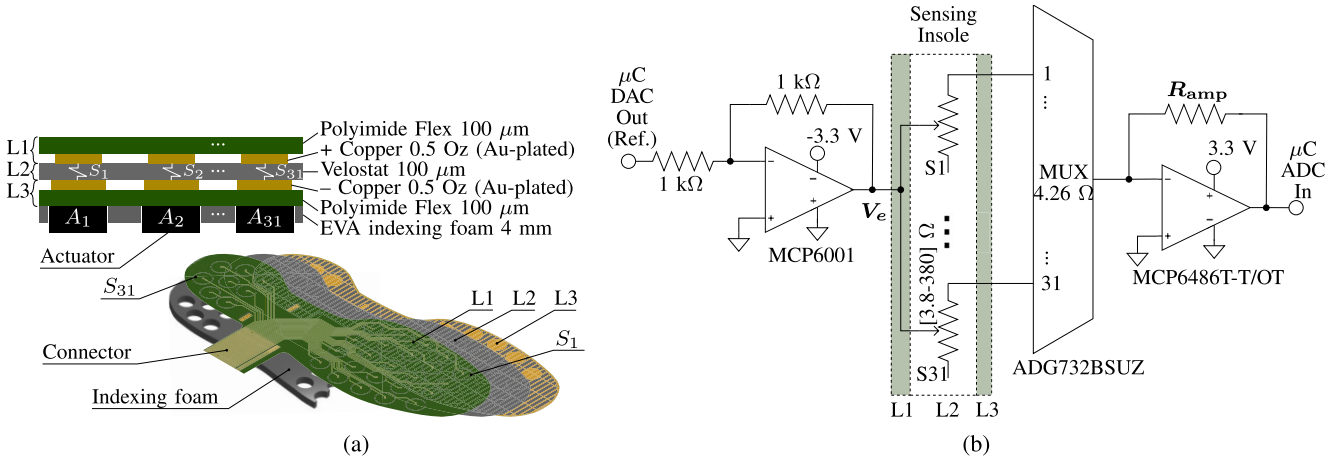

Fig. 1. Construction and sensing electronics for P-MAPS. (a) Layers. (b) Conditioning circuit.

STMicroelectronics) digital-to-analog converter (DAC) Out. In this way, it is possible to adjust the output characteristics of the amplifier on the right side on the fly, which scales the voltage measurement of the insole following equation:

$$V_{\text{out}} = \frac{-R_{\text{amp}}}{R_{\text{sense}} + R_{\text{MUX}}} \cdot V_e. \tag{1}$$

As such, the reference voltage V_e is inversely proportional to the output voltage V_{out}. The multiplexer (MUX) adds a series resistance (R_{MUX}) to the Velostat resistance R_{sense}. The amplifier gain, thus the output range, can be adjusted using R_{amp}. This electronic design enables resistance measurements without the need for a power-consuming voltage-divider resistor and helps to linearize the piezoresistive response within the input range of the microcontroller's analog-to-digital converter (ADC), through the selection of R_{amp}. All sensing-area electrodes are accessed by iteratively selecting channels through the MUX, whose single output feeds the second amplifier on the right side. The ability to vary the negative reference voltage (V_e) further allows compensation for resistance variations across the piezoresistive sheet, which arise primarily from manufacturing tolerances.

Finally, the value read by the microcontroller can be sent via Bluetooth to a PC, where it is recorded, or used directly onboard for the embedded offloading algorithm. For this purpose, a separate custom compact-sized PCB that can be integrated inside a shoe was developed. It includes both the sensor DAQ electronics and the additional electronics to control the offload actuators, which will be used in the future. Measurements are acquired at a sampling rate of 50 Hz, sufficient to capture the pressure peaks that occur during the gait cycle [31]. With this arrangement, it is possible to measure all areas with a transmission range of 20 m between the insole and the computer, which is comparable to that of commercial systems.

III. Sensor Characterization and Calibration

The sensing insole was characterized for resistivity range, hysteresis, repeatability, and drift. Although hysteresis and drift are parameters that do not affect dynamic gait measurements due to the nature of the loading (high frequency and repeated loading), they must be considered for calibration purposes and are therefore reported hereby. Finally, the coefficients of a third-order polynomial calibration equation were determined for each sensing area according to its pressure versus ADC value curve. Section III-A explain the process in detail.

A. Methods

The sensing insole was characterized and calibrated using the test bench shown in Fig. 2, the trublu system by Novel GmbH. This system is composed of a flexible membrane controlled by a pneumatic circuit that uniformly stimulates all areas of the sensing insole. An external pressure transducer from Honeywell (series PX3) measures pneumatic pressure, which is captured with a National Instruments DAQ USB-6221 at a frequency of 1 kHz.

1) Material Uniformity and Range: The tracks leading to the electrodes were designed to add the least amount of resistance, so that their length variations are negligible. This was corroborated by external measurements, in which the piezoresistive material in the sensor stack was replaced by a double-sided copper-clad board with a known resistance between the electrodes. Data from this experiment were also used to determine the values of R_{amp} and V_e required to capture the entire range of measurement of the material.

2) Hysteresis: To evaluate the hysteresis behavior of the pressure-sensing insole, a controlled loading–unloading experiment was performed. The objective was to quantify the extent of signal deviation between loading and unloading phases under identical applied pressures, thereby characterizing the insole's memory effect and nonlinear elastic response.

A quasi-static loading profile was applied, incrementally increasing the applied rig pressure from 0 to 400 kPa in 10-kPa steps, holding each load for 5 s to allow signal stabilization. Subsequently, the load was decreased from 400 to 0 kPa in identical steps.

At each pressure step, the corresponding sensor output was recorded at a sampling frequency of 50 Hz. The sensor response during the ascending (loading) and descending (unloading) phases was plotted against the applied pressure,

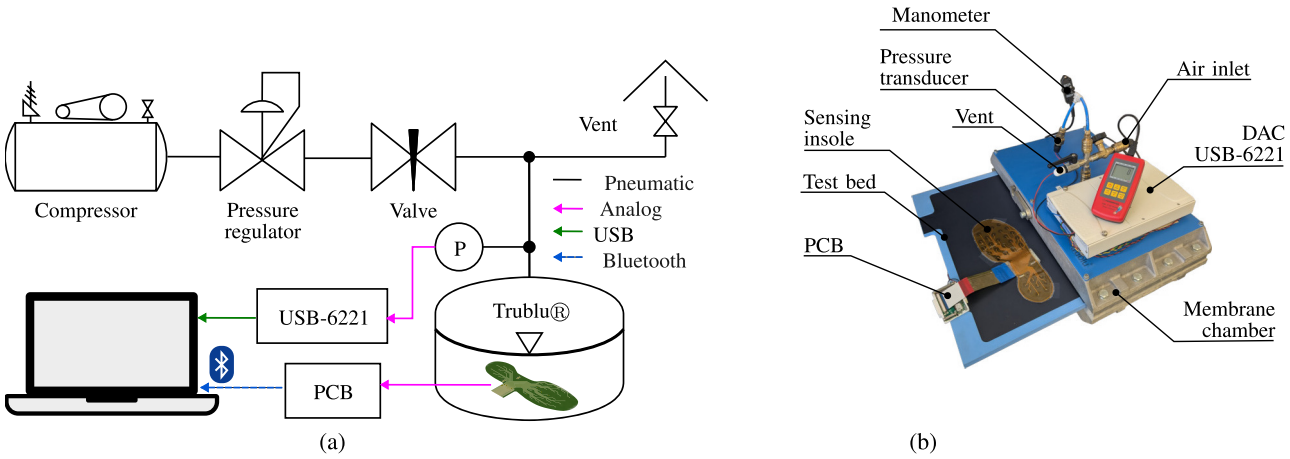

Fig. 2. Test bench used for the characterization and calibration of the sensing insole P-MAPS. (a) Block diagram of the test bench. (b) Arrangement of the test bench. During the trials, the test bed was slid closed so that it is contained inside the membrane chamber.

measured with the pneumatic pressure transducer, to generate a hysteresis loop, normalized per sensor ($V_{max} - V_{min}$). The magnitude of hysteresis (H_{norm}) was quantified as the maximum absolute difference in sensor output between loading and unloading at the same pressure level, normalized by the full-scale output level

$$H_{norm} = \frac{\max|V_{load}(P_i) - V_{unload}(P_i)|}{V_{max} - V_{min}} \quad (2)$$

where $V_{load}(P_i)$ and $V_{unload}(P_i)$ denote the ADC value during the loading and unloading phases at the load level P_i, respectively.

3) Repeatability: Repeatability was determined by applying three consecutive identical load–unload cycles (0–350 kPa) to the insole, using the same stepwise protocol described above. The coefficient of variation (CV) of the sensor output at each force step across trials was computed as a measure of repeatability

$$CV(P_i) = \frac{\sigma(P_i)}{\mu(P_i)} \quad (3)$$

where $\sigma(P_i)$ and $\mu(P_i)$ represent the standard deviation and mean of the sensor output at the load level P_i, respectively.

For each repeat dataset and sensor, the cycle waveforms were time-normalized to [0, 1], amplitude-normalized per sensor [min − max], and interpolated into a fixed grid. The curves are grouped by target pressure (approximately 60, 100, 150, 210, 250, and 300 kPa).

4) Drift: The drift was assessed by applying a constant load of 300 kPa to the same sensor site for a prolonged period of 5 min. The sensor output was continuously recorded at 50 Hz and the baseline drift was quantified as the percentage change in signal relative to the initial value after test-bench pressure and signal stabilization

$$\text{Drift} = \frac{V(t = 360\text{ s}) - V(t = 60\text{s})}{V(t = 60\text{s})}. \quad (4)$$

An initial 60-s stabilization period was excluded to avoid transient effects immediately after loading. This test was repeated three times to assess consistency and the drift was reported as mean ± standard deviation.

5) Pressure Calibration: For calibration, the full internal IOF assembly, including the actuators, was connected to replicate the measurement conditions as closely as possible. Because the custom PCB integrates both sensing and actuation circuits, the power drawn from the actuators could introduce baseline shifts or electromagnetic coupling in the pressure readings. To account for these effects, calibration was performed under realistic operating conditions, with the actuators maintained in their normally-ON state and drawing current from the control board. Then, a pneumatic pressure ramp of 50 kPa/min was applied to P-MAPS, while the ADC output was recorded at 50 Hz. The following 3rd-order polynomial equation was used to calibrate the ADC measurement of each area from either feet to pressure:

$$a_3x^3 + a_2x^2 + a_1x + a_0 = 0. \quad (5)$$

The coefficients a_3–a_0 were determined using National Instrument's Labview General Polynomial Fit VI, with the least squares method and the singular value decomposition algorithm, and a calibration file used during all gait experiments was recorded. Finally, the error at each pressure level was determined as the difference between the P-MAPS measured pressure and the externally measured pneumatic pressure, as a percentage of pneumatic pressure.

B. Results and Discussion

1) Range and Resistivity: When cycling through the different sensing areas using a known resistance between the electrodes, the voltage at the "μC ADC In" terminal remained fairly constant, as shown by the red line in Fig. 3. In contrast, when the piezoresistive material is inserted into the sensor stack and a constant pressure of 350 kPa is applied to all areas, the measured voltage varies between each pressure-sensing area (Fig. 3, blue line). This indicates that the resistance variations introduced by connectors, tracks, and vias in the sensing insole are negligible (red line) and that the resistivity of the piezoresistive material is not uniform across its surface (blue line). The resistance of the Velostat layer was observed to vary between 3.8 and 380 Ω, inversely proportional to the applied force. This experiment also allowed the determination

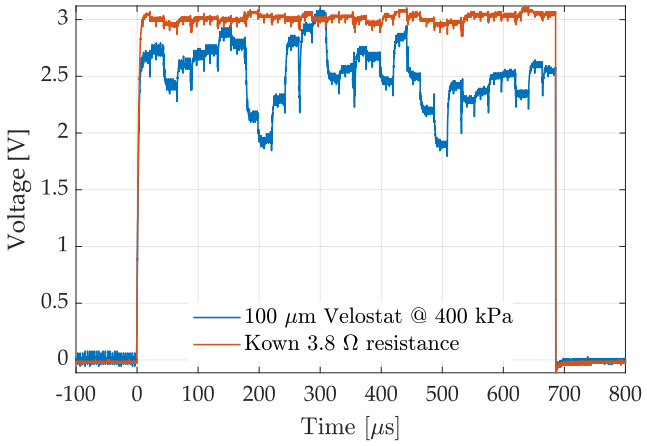

Fig. 3. Voltage while multiplexing through sensing areas.

of suitable values for R_{amp} and V_e to ensure full-range digitization of the material's response, which were set to $R_{\text{amp}} = 270\ \Omega$ and $V_e = -0.8$ V. In the future, a scheme that changes V_e to the most adequate value for each sensing area will be implemented, with the advantage of making the sensing current as constant as possible across the electrodes, minimizing the effect of thermal-induced heating and drift.

2) Hysteresis: Fig. 4(a) shows the results of the hysteresis characterization. The solid lines represent the grand mean across all sensors, while the shaded regions indicate the standard deviation. An aggregated hysteresis index H_{norm} of 25.8% was observed between the loading and unloading cycles. Although this value is relatively high, its impact is moderated under dynamic gait conditions because plantar loads typically follow a cyclic pattern from 0 to P_{peak} and back to 0, periodically unloading the sensing layers. This unloading reduces the accumulation of hysteresis effects between successive steps. However, during prolonged static loading conditions, such as standing, hysteresis can introduce additional uncertainty in the absolute pressure estimation. Nevertheless, for the intended application of plantar-pressure monitoring and IOF, the primary objective is the detection and mitigation of sustained high-pressure regions during gait rather than the precise quantification of absolute pressure. Consequently, relative pressure levels and spatial pressure distribution remain informative for the evaluation of ulceration risk and the offload control, although observed hysteresis must be considered when designing calibration and signal-processing strategies.

3) Repeatability: The repeatability results are shown in Fig. 4(b). The solid lines represent the mean response at different pressure levels, and the semi-transparent shaded regions denote the standard deviation. Narrower shaded bands indicate better repeatability. As shown, the sensors perform consistently throughout the 60–300-kPa range, with coefficients of variation between 0.81% and 2.34%. This level of repeatability is sufficient for the intended application.

4) Drift: Fig. 4(c) presents the drift characterization results, showing a drift of 6.35% after maintaining a constant load for 5 min. This drift is believed to arise from several sources: viscoelastic creep of the polymer (slow deformation of the material under sustained stress), carbon network densification (gradual compaction of conductive particles forming new conduction paths), polymer stress relaxation feedback (redistribution of internal stresses that alter local contact pressures), and environmental coupling (effects of temperature or humidity on material behavior) [32]. Although such a drift has minimal impact during gait, remaining below 0.01% over the short duration of a single step (Fig. 4(c), single step inset plot), it becomes an important factor during calibration procedures. Therefore, calibration must be performed using a rig that applies a uniform and stable pressure across all sensing areas, as done in this study, to ensure that drift-induced bias is minimized.

5) Pressure Calibration: Fig. 5(a) presents the calibration curves for all sensing areas in the 0–400-kPa range, with each line corresponding to a different sensing location. Fig. 5(b) shows the error that results after fitting a third-order polynomial to the response of each area. Both plots highlight the nonuniformity of the material previously illustrated in Fig. 3, as the sensing areas exhibit noticeably different outputs under identical applied pressures. Data also reveal that pressures below approximately 50 kPa exhibit reduced precision, likely because sensor layers do not achieve full mechanical contact at such low loads, leading to unstable resistance readings. Since pressures in this range are uncommon during gait, values below that threshold are excluded from subsequent analyses but still included for calibration purposes.

IV. Gait Measurements

To evaluate the dynamic performance, accuracy, and precision of the custom-built pressure-sensing insole, a comparative analysis was performed against a commercially available gold-standard insole (Pedar and Novel), which features full plantar coverage and high-resolution sensing. The comparison focused on relative pressure profiles and signal consistency during gait. For these tests, the full IOF was used with the offloading components blocked to reproduce plantar-pressure readings under real-world conditions.

A. Methods

A stack configuration was adopted for the simultaneous collection of P-MAPS and Pedar data on the same foot during walking. The P-MAPS insole was placed directly above the IOF offloading components, with the Pedar insole on top, and both were secured using double-sided adhesive tape to minimize displacement, as illustrated in Fig. 6.

Four healthy adult participants wore the stacked insoles inside the IOF and walked a 5-m linear path for approximately 20 s per trial, maintaining a self-selected pace. A total of six trials were recorded. Pressure data from both systems were acquired simultaneously using an electronic trigger to account for communication latency.

The raw signals were resampled at 50 Hz and smoothed using a 50-ms moving-average filter. Residual clock offsets between systems were corrected by maximizing the amplitude-weighted Pearson cross correlation between candidate sensor pairs within a ±0.5-s search window, with the optimal lag applied to the P-MAPS time axis.

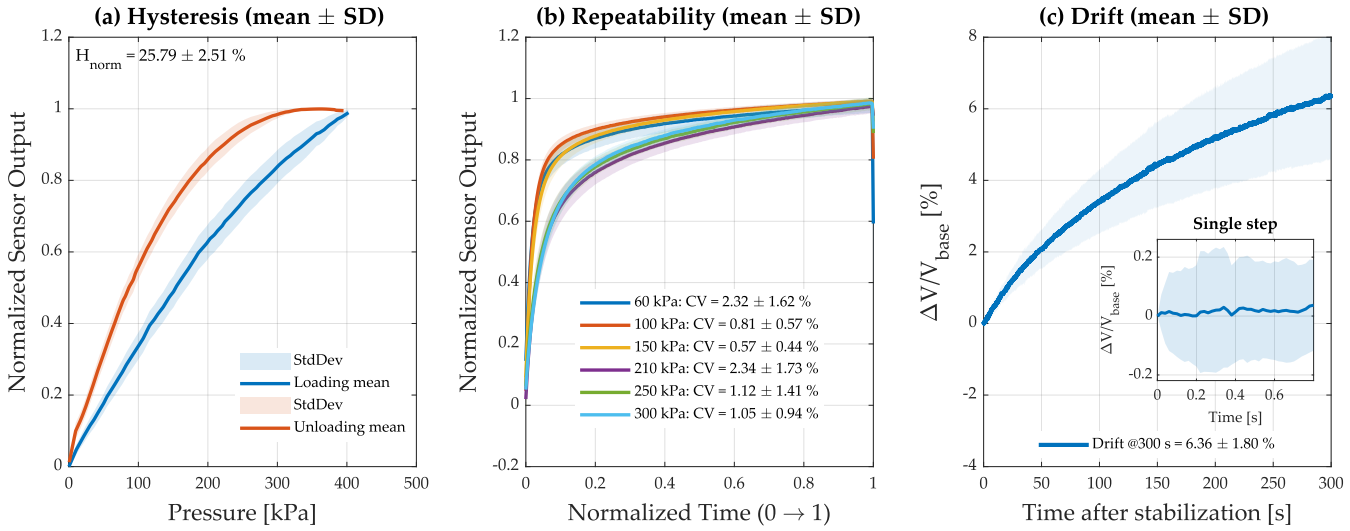

Fig. 4. Aggregate characterization across all sensing areas. (a) Hysteresis. (b) Repeatability. (c) Drift.

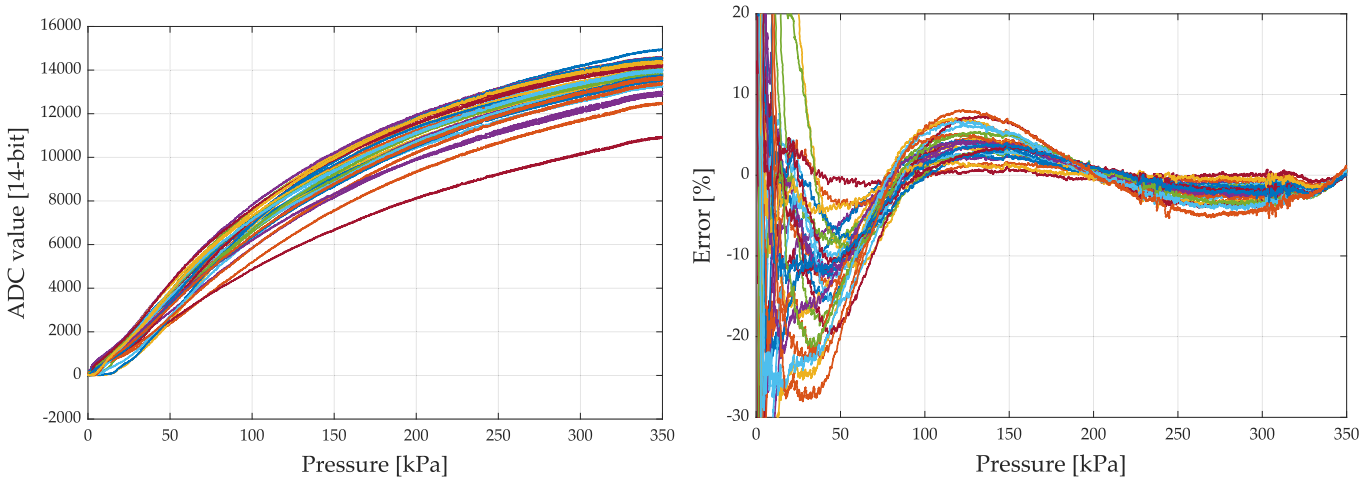

Fig. 5. Calibration (left) and error (right) plots. Each color line represents the measurement from each sensing area.

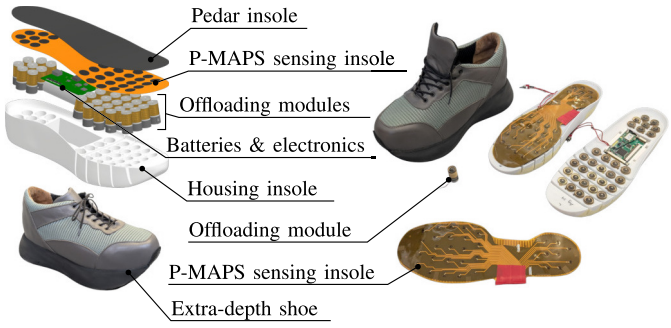

Fig. 6. IOF prototype, including sensing, controlling, and actuating components.

The initial sensor correspondence was established using the known P-MAPS geometry and the Pedar sensor layout. Due to variations in assembly and gait-induced misalignment, a postprocessing step was applied to refine alignment. A rigid per-foot transform (dx, dy, and $d\theta$) was optimized to minimize overlap-weighted normalized root mean square error (NRMSE) between candidate pairs, subject to a regularization penalty; it was accepted only if it improved the NRMSE by at least 5% over the nominal orientation. Sensor pairs were selected using a hybrid approach that combined geometric overlap prefiltering and NRMSE-based one-to-one assignment. Pairs were excluded if Pearson $r < 0.5$ or if the mean peak Pedar pressure was below 40 kPa. The per-step peak pressure error and the pressure–time integral (PTI) error were computed for each retained pair. The temporal correlation r and the NRMSE were evaluated in the analysis window

$$\mathrm{NRMSE} = \frac{\sqrt{\frac{1}{N}\sum_{i=1}^{N}\left(P_{\text{P-MAPS}}(i) - P_{\text{Pedar}}(i)\right)^2}}{P_{\text{Pedar,max}} - P_{\text{Pedar,min}}}. \quad (6)$$

The topology of the P-MAPS sensing regions is shown in Fig. 7. For a European size 43 shoe, the sensing areas used in the analysis are highlighted in blue, and the corresponding sensors are listed in Table II.

B. Results and Discussion

P-MAPS demonstrated dynamic performance comparable to that of the Pedar system. Fig. 8 shows a strong correspondence

TABLE II
SENSOR PAIRS INCLUDED IN THE ANALYSIS WITH MEAN GEOMETRIC OVERLAP ACROSS CONTRIBUTING TRIALS (ALIGNED GEOMETRY). OVERLAP IN %. REGIME (REG.) BASED ON ERROR

Left					Right				
Pedar	P-MAPS	Overlap (%)	n	Reg.	Pedar	P-MAPS	Overlap (%)	n	Reg.
L76	L9	100.0	3	AA	R76	R5	100.0	4	G
L75	L10	99.1	5	AA	R75	R14	100.0	3	HW
L79	L7	97.9	5	G	R79	R7	92.7	3	G
L14	L26	88.2	3	G	R14	R24	92.5	4	G
L73	L11	73.9	4	G	R72	R12	95.5	1	G

G = geometry-predictable; AA = area-averaging dominated; HW = hardware outlier.
n = number of contributing trials.

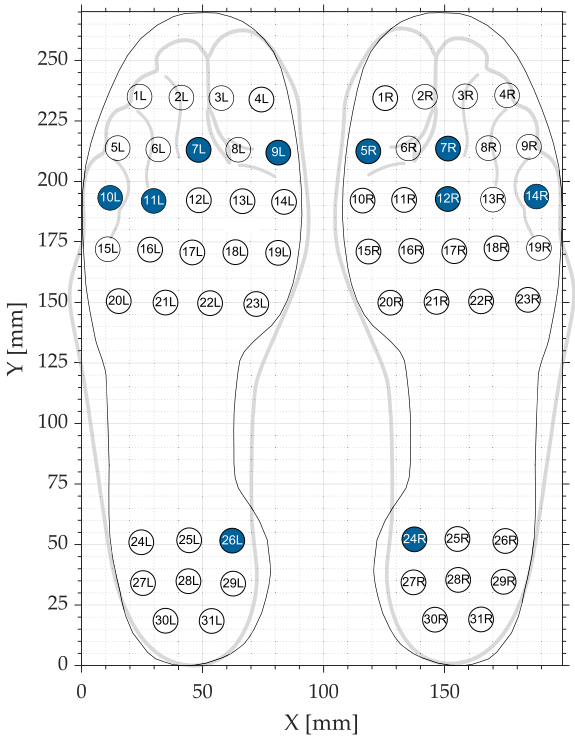

Fig. 7. Custom P-MAPS sensing-area topology. Areas used for the analysis are highlighted in blue. Anatomical, to-scale foot imprints adapted from [33].

between the two measurements throughout the gait cycle. Because the P-MAPS layers are not bonded, pressures below approximately 30 kPa show reduced reliability, particularly during unloading, as visible in measurements below 40 kPa for the P-MAPS R7 signal. This behavior is consistent with the low-pressure performance observed during sensor characterization. However, this limitation has minimal impact on the intended application, as clinically relevant PPs for the assessment of the risk of DFU and the offload control typically exceed 200–300 kPa. The reduced accuracy at very low loads affects mainly phases where the foot is partially or fully unloaded, which are not critical to identifying high-pressure regions or guiding offloading. Despite this limitation, both systems exhibit similar temporal behavior, with P-MAPS showing a slightly longer time constant, visible as less steep rising and

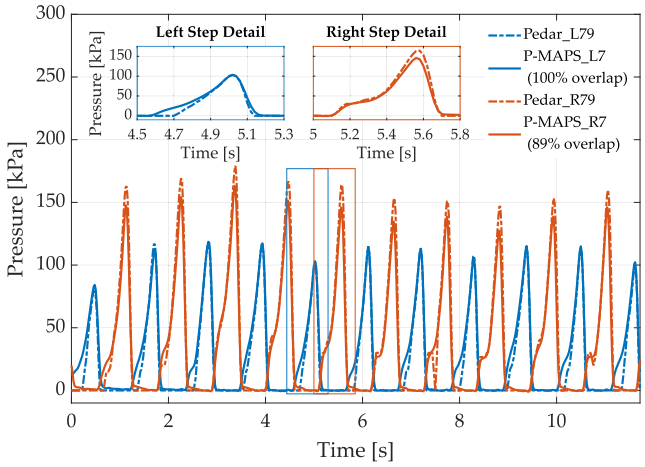

Fig. 8. Example time-series measurements from Pedar (dotted lines) and P-MAPS (solid lines) for the left (blue) and right (red) feet. The traces correspond to sensors overlapping in the central forefoot region: Pedar L79 aligned with P-MAPS L7 (97.9% overlap) and Pedar R79 aligned with P-MAPS R7 (92.7% overlap).

falling edges in the inset plots. A brief pressure drop in the Pedar R79 trace around 7.5 s is likely due to a missing data packet and is not reflected in the P-MAPS measurement.

The readings from both feet originate from anatomically similar regions; however, the right foot shows a consistently higher peak pressure, approximately 40 kPa above the left, reflecting natural asymmetries arising from the individual gait mechanics of the participant. This variation emphasizes the intrinsic subject-specific nature of plantar-pressure patterns, and the fact that they are observed in both systems confirms that the differences are biomechanical rather than sensor-related. Furthermore, the dynamic limitations reported in Section III, namely hysteresis and drift, are not perceptible during the gait cycle, indicating that the current design is adequate for the intended application.

The apparent error for the peak of Pedar R79 versus P-MAPS R7 in Fig. 8 can be traced to residual geometric mismatch between the two insoles. This tendency is quantified in Fig. 9(a), which shows the aggregate agreement of the peak pressure over six trials. Pairs with high spatial overlap and small centroid offset, such as R76/R5 and L79/L7, consistently achieve peak errors below 5%, confirming that geometric colocalization reliably predicts measurement agreement. However, pairs such as L76/L9 exhibit large reproducible peak errors (34%–38%) despite near-perfect geometric overlap. This reflects an area-average effect: the Pedar cell integrates pressure over approximately 190 mm^2, while the P-MAPS sensor samples a 79-mm^2 area located near the maximum intracell pressure. In this regime, P-MAPS captures the true local peak while Pedar reports a spatially averaged underestimate, a structural consequence of Pedar's sensor geometry.

For this analysis, three error regimes are defined. Geometry-predictable pairs (gray) exhibit a median absolute peak error below 15%, indicating that agreement is primarily governed by spatial overlap (e.g., R76/R5, R79/R7, and L73/L11). Area-averaging dominated pairs (amber) show median errors above 15% in multiple trials despite a low geometric mismatch

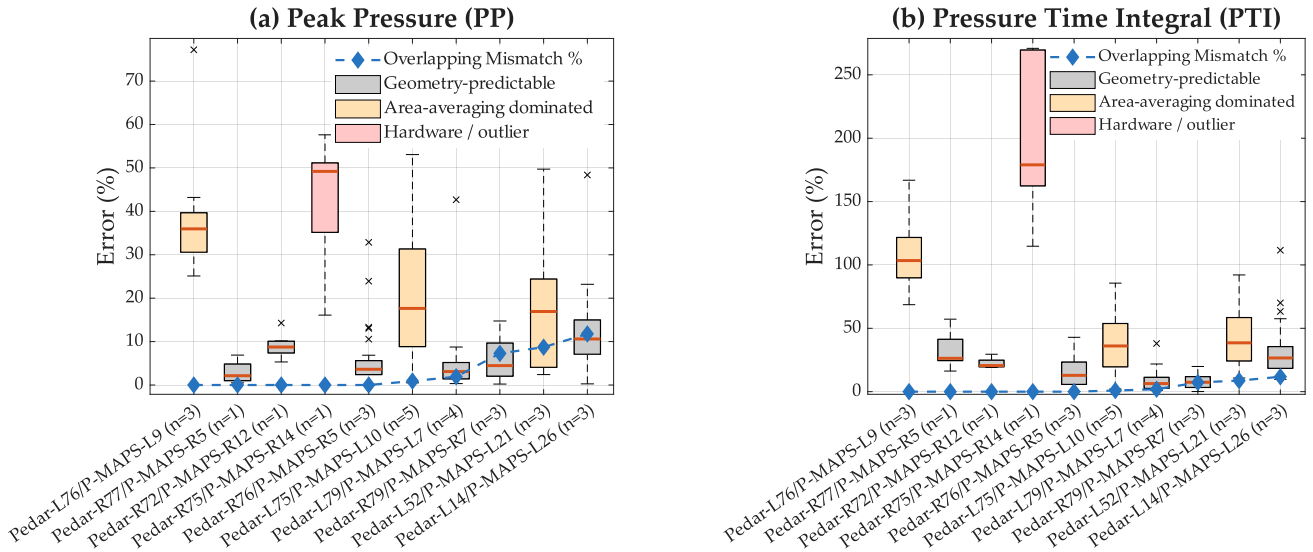

Fig. 9. Aggregate error between Pedar and P-MAPS across all trials (a) per-step peak pressure and (b) per-step PTI. Each box shows the interquartile range across all contributing steps and trials, with the median indicated by the orange line. The dashed blue diamond line represents the geometric overlap mismatch, defined as the percentage of the P-MAPS sensing area extending beyond its paired Pedar cell. Box color indicates the dominant error regime: gray denotes geometry-predictable error correlated with overlap mismatch; amber denotes reproducible error despite low geometric mismatch, attributed to spatial averaging within the larger Pedar cell at anatomical pressure maxima; and red denotes outlier pairs from a single trial with anomalously high error, suggesting hardware-related effects rather than geometric causes. The number of contributing trials is indicated as (n = x) for each pair.

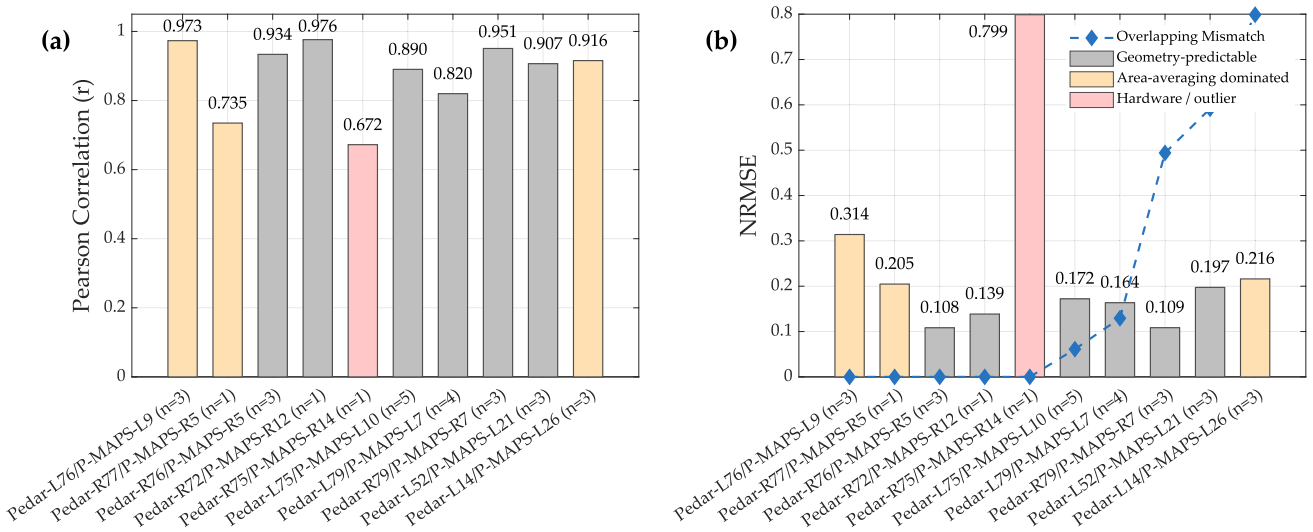

Fig. 10. Aggregate temporal agreement between Pedar and P-MAPS across all trials (a) whole-series Pearson correlation and (b) NRMSE. Bars indicate the mean across contributing trials, with values labeled above each bar. Bar colors follow the regime classification in Fig. 9: gray, geometry-predictable; amber, area-averaging dominated; red, hardware outlier. In (b), the dashed blue diamond line represents the geometric overlap mismatch normalized to the NRMSE scale, enabling direct comparison between signal disagreement and spatial misalignment. The number of contributing trials is indicated as (n = x) for each case.

(e.g., L76/L9), reflecting intrinsic differences in the sensing area that are not related to alignment. Finally, hardware outliers (light red) correspond to isolated cases (n = 1) with median errors exceeding 30% (e.g., R75/R14), attributed to transient sensor or acquisition effects rather than geometric causes.

The PTI errors in Fig. 9(b) show a broader distribution, as expected. PTI integrates pressure over the full stance phase and is sensitive to differences in sensor dynamics, response time, and hysteresis intrinsic to each technology. The PTI metric is therefore presented as a system-level loading indicator rather than a direct accuracy measure. Fig. 10(a) and (b) shows aggregate temporal correlation and NRMSE in all trials. The consistent ranking of sensor pairs, with most achieving $r > 0.85$, confirms that performance is governed primarily by anatomical placement rather than trial-specific conditions.

In general, these results highlight the importance of targeted sensing-area design in plantar-pressure instrumentation. Without sensing regions that correspond to the locations of the offload actuators, the relationship between measured pressure and actuator-specific loading becomes ambiguous, reducing the reliability of ulcer risk assessment and offload performance evaluation.

V. Conclusion and Future Work

This article presented the design and characterization of P-MAPS, a custom-topology plantar-pressure-sensing insole suitable for full integration into IOF. The proposed design demonstrated improved hysteresis and drift performance compared to previous reports. The measured operating range of 45–350 kPa and the repeatability (coefficient of variation below 2.5%) enable the acquisition of high-quality gait pressure data comparable to the Pedar gold-standard system.

Gait experiments across multiple participants further confirmed consistent sensing behavior and strong agreement with Pedar measurements under dynamic conditions. Dynamic tests also highlighted the importance of a strict calibration protocol: observed drift (6% after 5 min) and hysteresis (25.8%) emphasize the need for uniform loading conditions and adequate recovery time to account for viscoelastic effects. The results also demonstrate the importance of spatial alignment between sensing regions and actuator modules for automatic offloading, strengthening the advantage of the customizable sensor topology implemented in P-MAPS. However, because the sensing layout does not fully cover the plantar surface, some loads may remain unmeasured; although elevated actuator profiles partially mitigate this effect, future work will extend the design to full plantar coverage.

In general, this work provides three main contributions. First, we quantified the effect of nonoverlapping sensor configurations on peak pressure detection accuracy, demonstrating how insufficient overlap can misrepresent hotspot magnitudes and compromise automatic pressure-redistribution algorithms. Second, we showed that a fully custom, low-cost sensing topology can achieve dynamic performance comparable to that of a gold-standard commercial system, providing a scalable pathway for application-specific plantar-pressure sensing. We also presented the associated electronic and topological design that enables this performance. Third, we characterized Velostat as a sensing material, evaluating its hysteresis, drift, and repeatability under controlled loading conditions and quantifying the calibration requirements necessary for reliable measurements.

Future work will investigate the long-term robustness of the sensing system under environmental and mechanical conditions typical of footwear use. In particular, the influence of temperature variations, humidity and perspiration, and repeated cyclic bending on the stability of the piezoresistive sensing elements will be evaluated. Although the flexible layered construction of P-MAPS is designed to accommodate deformation and provide partial protection from environmental exposure, extended durability testing under controlled climatic and mechanical conditions will be required to quantify long-term performance and guide future design refinements.

Future work will also incorporate shear-stress detection to enable richer multimodal risk indicators combining PP, shear loading, and PTI to detect earlier the risk of DFU. Additionally, P-MAPS will be used to evaluate the effectiveness of offloading modules under real-world conditions, advancing toward autonomous offloading interventions that do not require patient action and ultimately reducing the incidence of DFU and associated amputations.

References

[1] International Diabetes Federation. (2025). *IDF Diabetes Atlas*. [Online]. Available: https://diabetesatlas.org

[2] D. G. Armstrong, A. J. M. Boulton, and S. A. Bus, "Diabetic foot ulcers and their recurrence," *New England J. Med.*, vol. 376, no. 24, pp. 2367–2375, Jun. 2017. [Online]. Available: https://www.nejm.org/doi/pdf/10.1056/NEJMra1615439

[3] J. Apelqvist, J. Larsson, and C.-D. Agardh, "Long-term prognosis for diabetic patients with foot ulcers," *J. Internal Med.*, vol. 233, no. 6, pp. 485–491, Jun. 1993. [Online]. Available: https://onlinelibrary.wiley.com/doi/pdf/10.1111/j.1365-2796.1993.tb01003.x.

[4] M. Lepäntalo et al., "Chapter V: Diabetic foot," *Seminars Vascular Surgery*, vol. 42, pp. S60–S74, Sep. 2010. [Online]. Available: https://www.sciencedirect.com/science/article/pii/S10785884116001 29

[5] S. L. Hemler et al., "Intelligent plantar pressure offloading for the prevention of diabetic foot ulcers and amputations," *Frontiers Endocrinology*, vol. 14, 2023, Art. no. 1166513. [Online]. Available: https://www.frontiersin.org/journals/endocrinology/articles/10.3389/fendo.2023.1166513/full

[6] A. Veves, H. J. Murray, M. J. Young, and A. J. M. Boulton, "The risk of foot ulceration in diabetic patients with high foot pressure: A prospective study," *Diabetologia*, vol. 35, no. 7, pp. 660–663, Jul. 1992, doi: 10.1007/bf00400259.

[7] S. A. Bus, D. G. Armstrong, R. W. van Deursen, J. E. A. Lewis, C. F. Caravaggi, and P. R. Cavanagh, "IWGDF guidance on footwear and offloading interventions to prevent and heal foot ulcers in patients with diabetes," *Diabetes/Metabolism Res. Rev.*, vol. 32, no. S1, pp. 25–36, Jan. 2016. [Online]. Available: https://onlinelibrary.wiley.com/doi/pdf/10.1002/dmrr.2697.

[8] Novel. (2025). *Footwear Pressure Distribution Measurement-Pedar*. [Online]. Available: https://novel.de/products/pedar/Footwear

[9] Tekscan. (2024). *F-Scan Go System Datasheet*. [Online]. Available: https://www.tekscan.com/sites/default/files/2024-05/240514_Tekscan_FScanGO_SystemFlyer_Final.pdf

[10] Moticon ReGo AG. (2023). *Opengo Sensor Insoles: Programmer's Guide*. [Online]. Available: https://moticon.com/wp-content/uploads/2023/09/AN-002-OpenGo-Programmers-Guide-A4-EN-03.04.pdf

[11] J. Tang et al., "A wearable insole system to measure plantar pressure and shear for people with diabetes," *Sensors*, vol. 23, no. 6, p. 3126, Mar. 2023. [Online]. Available: https://www.mdpi.com/1424-8220/23/6/3126

[12] B. Tiwari et al., "A polyester–nylon blend plantar pressure sensing insole for person with diabetes," *IEEE Sensors Lett.*, vol. 8, no. 1, pp. 1–4, Jan. 2024. [Online]. Available: https://ieeexplore.ieee.org/abstract/document/10336846

[13] R. de Fazio, E. Perrone, R. Velázquez, M. De Vittorio, and P. Visconti, "Development of a self-powered piezo-resistive smart insole equipped with low-power BLE connectivity for remote gait monitoring," *Sensors*, vol. 21, no. 13, p. 4539, Jul. 2021, doi: 10.3390/s21134539.

[14] X. Hu et al., "A low-cost instrumented shoe system for gait phase detection based on foot plantar pressure data," *IEEE Sensors J.*, vol. 23, no. 18, pp. 20729–20738, 2023, doi: 10.1109/JTEHM.2023.3319576.

[15] S. A. Bus, J. S. Ulbrecht, and P. R. Cavanagh, "Pressure relief and load redistribution by custom-made insoles in diabetic patients with neuropathy and foot deformity," *Clin. Biomechanics*, vol. 19, no. 6, pp. 629–638, Jul. 2004.

[16] B. Latsch et al., "Sensor insoles: A review," 2025, *arXiv:2509.00260*.

[17] L. Wang et al., "A review of wearable sensor systems to monitor plantar loading in the assessment of diabetic foot ulcers," *IEEE Trans. Biomed. Eng.*, vol. 67, no. 7, pp. 1989–2004, Jul. 2020. [Online]. Available: https://ieeexplore.ieee.org/document/8944053/

[18] P. Castro-Martins, A. Marques, L. Coelho, M. Vaz, and J. S. Baptista, "In-shoe plantar pressure measurement technologies for the diabetic foot: A systematic review," *Heliyon*, vol. 10, no. 9, May 2024, Art. no. e29672. [Online]. Available: https://linkinghub.elsevier.com/retrieve/pii/S2405844024057037

[19] Q. Zhang, Y. L. Wang, Y. Xia, X. Wu, T. V. Kirk, and X. D. Chen, "A low-cost and highly integrated sensing insole for plantar pressure measurement," *Sens. Bio-Sensing Res.*, vol. 26, Nov. 2019, Art. no. 100298. [Online]. Available: https://www.sciencedirect.com/science/article/pii/S2214180419300674

[20] J. Gao et al., "Smart insole: Stand-alone soft 3-axis force sensing array in a shoe," in *Proc. IEEE SENSORS*, Oct. 2023, pp. 1–4. [Online]. Available: https://ieeexplore.ieee.org/document/10324863/

[21] B. Ren and J. Liu, "Design of a plantar pressure insole measuring system based on modular photoelectric pressure sensor unit," *Sensors*, vol. 21, no. 11, p. 3780, May 2021. [Online]. Available: https://www.mdpi.com/1424-8220/21/11/3780

[22] D. R. McArthur et al., "Dynamic shear and normal force detection in a soft insole using hybrid optical & piezoresistive sensors," in *Proc. 10th IEEE RAS/EMBS Int. Conf. Biomed. Robot. Biomechatronics (BioRob)*, Jun. 2024, pp. 370–375. [Online]. Available: https://ieeexplore.ieee.org/abstract/document/10719944

[23] R. A. Lakho, Z. Yi-Fan, J. Jin-Hua, H. Cheng-Yu, and Z. Ahmed Abro, "A smart insole for monitoring plantar pressure based on the fiber Bragg grating sensing technique," *Textile Res. J.*, vol. 89, no. 17, pp. 3433–3446, Sep. 2019, doi: 10.1177/0040517519833977.

[24] L. Wang et al., "A portable insole system to simultaneously measure plantar pressure and shear stress," *IEEE Sensors J.*, vol. 22, no. 9, pp. 9104–9113, May 2022. [Online]. Available: https://ieeexplore.ieee.org/document/9743438

[25] X. Li, K. Wang, Y. L. Wang, and K. C. Wang, "Plantar pressure measurement system based on piezoelectric sensor: A review," *Sensor Rev.*, vol. 42, no. 2, pp. 241–249, Mar. 2022. [Online]. Available: http://www.emerald.com/sr/article/42/2/241-249/341778

[26] S. Rajala, R. Mattila, I. Kaartinen, and J. Lekkala, "Designing, manufacturing and testing of a piezoelectric polymer film in-sole sensor for plantar pressure distribution measurements," *IEEE Sensors J.*, vol. 17, no. 20, pp. 6798–6805, Oct. 2017. [Online]. Available: http://ieeexplore.ieee.org/document/8030036/

[27] F. He, X. You, W. Wang, T. Bai, G. Xue, and M. Ye, "Recent progress in flexible microstructural pressure sensors toward human–machine interaction and healthcare applications," *Small Methods*, vol. 5, no. 3, Mar. 2021, Art. no. 2001041. [Online]. Available: https://onlinelibrary.wiley.com/doi/10.1002/smtd.202001041

[28] S. Xu et al., "Recent advances in flexible piezoresistive arrays: Materials, design, and applications," *Polymers*, vol. 15, no. 12, p. 2699, Jun. 2023. [Online]. Available: https://www.mdpi.com/2073-4360/15/12/2699

[29] Y. Huang, X. Fan, S.-C. Chen, and N. Zhao, "Emerging technologies of flexible pressure sensors: Materials, modeling, devices, and manufacturing," *Adv. Funct. Mater.*, vol. 29, no. 12, Mar. 2019, Art. no. 1808509. [Online]. Available: https://advanced.onlinelibrary.wiley.com/doi/10.1002/adfm.201808509

[30] Y. Tan et al., "A soft wearable and fully-textile piezoresistive sensor for plantar pressure capturing," *Micromachines*, vol. 12, no. 2, p. 110, Feb. 2021. [Online]. Available: https://www.mdpi.com/2072-666X/12/2/110

[31] M. N. Orlin and T. G. McPoil, "Plantar pressure assessment," *Phys. Therapy*, vol. 80, no. 4, pp. 399–409, Apr. 2000. [Online]. Available: https://academic.oup.com/ptj/article/80/4/399/2842449

[32] S. Domínguez-Gimeno, C. Medrano-Sanchez, R. Igual-Catalan, and I. Plaza-Garcia, "Optimized creep-hysteresis model to improve center-of-pressure detection in pressure-sensitive mats," *IEEE Sensors J.*, vol. 25, no. 9, pp. 15295–15306, May 2025. [Online]. Available: https://ieeexplore.ieee.org/document/10932676/

[33] G. Rogati, A. Leardini, M. Ortolani, and P. Caravaggi, "Semi-automatic measurements of foot morphological parameters from 3D plantar foot scans," *J. Foot Ankle Res.*, vol. 14, no. 1, p. 18, Jan. 2021. [Online]. Available: https://onlinelibrary.wiley.com/doi/10.1186/s13047-021-00461-z